RAA 2015 Vol. **15** No. **11**, 1905–1916 doi: 10.1088/1674–4527/15/11/012
http://www.raa-journal.org *http://www.iop.org/journals/raa*

Research in Astronomy and Astrophysics

Point source detection performance of Hard X-ray Modulation Telescope imaging observation

Zhuo-Xi Huo[1,2], Yi-Ming Li[3], Xiao-Bo Li[5] and Jian-Feng Zhou[2,4]

[1] Department of Physics, Tsinghua University, Beijing 100084, China; *huozx@tsinghua.edu.cn*
[2] Centre for Astrophysics, Tsinghua University, Beijing 100084, China
[3] Laboratoire de l'Accélérateur Linéaire, Orsay 91898, France
[4] Department of Engineering Physics, Tsinghua University, Beijing 100084, China
[5] Institute of High Energy Physics, Chinese Academy of Sciences, Beijing 100049, China

Received 2014 November 23; accepted 2015 April 14

Abstract The Hard X-ray Modulation Telescope (HXMT) will perform an all-sky survey in the hard X-ray band as well as deep imaging of a series of small sky regions. We expect various compact objects to be detected in these imaging observations. Point source detection performance of HXMT imaging observation depends not only on the instrument but also on the data analysis method that is applied since images are reconstructed from HXMT observed data with numerical methods. The denoising technique used plays an important part in the HXMT imaging data analysis pipeline along with demodulation and source detection. In this paper we have implemented several methods for denoising HXMT data and evaluated the point source detection performances in terms of sensitivities and location accuracies. The results show that direct demodulation with 1-fold cross-correlation should be the default reconstruction and regularization method, although both sensitivity and location accuracy could be further improved by selecting and tuning numerical methods in data analysis used for HXMT imaging observations.

Key words: methods: data analysis — methods: numerical — techniques: image processing — instrumentation: high angular resolution

1 INTRODUCTION

1.1 Background

The Hard X-ray Modulation Telescope (HXMT) is a planned Chinese space X-ray telescope. The telescope will perform an all-sky survey in the hard X-ray band (1 – 250 keV), and a series of deep imaging observations in small sky regions and pointed observations.

We expect a large number of X-ray sources, e.g., AGNs, to be detected in the all-sky survey. We also expect that, through a series of deep imaging observations in the Galactic plane, X-ray transients can be detected (Li 2007; Lu 2012). Therefore the point source detection performance is one of our concerns related to HXMT data analysis.

Methods and corresponding sensitivities of pointed observation have been discussed by Jin et al. (2010). In imaging observations such as the all-sky survey and deep imaging of small sky regions, a variety of issues related to data analysis and methods are involved.

First, images are computed instead of recorded directly by the optical instrument. Mapping as well as image reconstruction methods are useful. The direct scientific data products from imaging observations of HXMT are all scientific events, more specifically, X-ray photon arrival events. The attitude control system of the spacecraft periodically reports the state of its attitude. We take these reported attitudes as nodes to perform certain interpolations to determine the instantaneous attitude for each scientific event. In this way, a set of parameters is assigned to each event, including the coordinates on the celestial sphere at which the telescope is pointing. Hence we call this process *event mapping*, where scientific events are mapped from the time domain to the celestial sphere. The product of this process is referred to as the observed image, which implies the dimensionality of the data.

Second, the exposure to a specific source is limited more strictly thus the signal-to-noise ratio (SNR) is tightly restricted. Hence regularization methods become important.

Finally, a picture is worth a thousand words. Various types of information can be extracted from an image by numerical methods.

In this paper we investigate the point source detection performance of the imaging and detecting system utilized by the telescope as well as diverse combinations of data analysis methods, especially regularization methods.

1.2 Modulation in HXMT Imaging Observation

The point spread function (PSF) of HXMT HE (High Energy Telescope), which is a sub-telescope of HXMT that is a composite telescope consisting of 18 collimated detectors, describes the response of the telescope to a point source when the telescope is pointing toward the source as well as different locations around it. In other words, the PSF is a density function of the distribution of responses occurring in a different observation state, which is denoted by the instantaneous attitude of the telescope in its orbit. So, the PSF takes the attitude of the telescope as its input.

We use the proper Euler's angles to describe the attitude of the telescope, i.e., ϕ and θ are the longitude and latitude of the pointing respectively, and ψ denotes the rotation angle of the telescope around its own pointing axis, namely, the position angle. The modulation equation that corresponds to the imaging observation over the spherical surface is

$$d(\phi,\theta,\psi) = \iint\limits_{\Omega} p(\phi,\theta,\psi,\phi',\theta') f(\phi',\theta') \cos\theta' \mathrm{d}\phi' \mathrm{d}\theta' \,, \tag{1}$$

where $f(\phi',\theta')$ is the object function (i.e., the image) defined in a compact subset of the spherical surface Ω, $p(\phi,\theta,\psi,\phi',\theta')$ is the modulation kernel function that relates the value of the object function $f(\phi',\theta')$ defined on a neighborhood of the point (ϕ',θ') in the subset Ω to the instantaneous response of the telescope, while its status is (ϕ,θ,ψ).

The modulation kernel function is determined by the PSF of the telescope. Suppose a unit point source is located at the zenith of the celestial sphere, i.e., the point $(0,0,1)$ in the corresponding Cartesian coordinate system. Fix the position angle ψ, while slewing the telescope across the polar cap, and assign responses of the telescope to the unit source to pixels on the celestial sphere. Then we obtain a map $P(\phi,\theta)$ representing the PSF on the celestial sphere with fixed rotation angle ψ.

The map is then projected to a tangent plane of the celestial sphere $z = 1$ by a gnomonic projection, i.e.,

$$\begin{cases} u = \cot\theta\cos\phi \,, \\ v = \cot\theta\sin\phi \,, \end{cases} \tag{2}$$

where u and v are local Cartesian coordinates on the tangent plane. Now we have

$$P_{\tan}(u,v) = P_{\tan}(\cot\theta\cos\phi, \cot\theta\sin\phi) = P(\phi,\theta) \,, \tag{3}$$

i.e., the PSF is defined on the tangent plane.

To provide for data analysis we have two discrete forms of $P_{\rm tan}$,

$$P_{i,j} = \frac{\iint_{\alpha_{i,j}} P_{\rm tan}(u,v){\rm d}u{\rm d}v}{\iint_{\alpha_{i,j}} {\rm d}u{\rm d}v}\,, \tag{4}$$

where $\alpha_{i,j}$ is the neighborhood of the pixel (i,j) in the 2-D pixel grid, and the normalized form

$$H_{i,j} = \frac{\iint_{\alpha_{i,j}} P_{\rm tan}(u,v){\rm d}u{\rm d}v}{\iint P_{\rm tan}(u,v){\rm d}u{\rm d}v}\,. \tag{5}$$

Given the discrete image $\boldsymbol{F}$, the detection area A and the duration of exposure on each pixel τ, the observed data are

$$\boldsymbol{D} = \tau \cdot \left[\frac{A}{\max\limits_{i,j} H_{i,j}} (\boldsymbol{F} * \boldsymbol{H}) + r_{\rm b} \right], \tag{6}$$

where $r_{\rm b}$ is the constant background count rate, $*$ denotes the convolution, and $\boldsymbol{H}$ is the normalized PSF on the tangent plane. Equation (6) approximates modulations in HXMT imaging observations.

Distortion occurs when projecting a set of points from (or to) a spherical surface to (or from) a plane. For example, in this process, the distance between any two points, the area of any continuous subset, and the angle between any two crossing lines (or tangents of curves) are altered non-uniformly. On the other hand, the rotation angle ψ is not always fixed during HXMT imaging observations. Both distortions in image reconstruction from HXMT observed data and rotations during imaging observations have been discussed by Huo & Zhou (2013). Here for the sake of simplicity, we ignore them in this article.

2 NUMERICAL METHODS

2.1 Single Point Source Detection Performance Estimation

We estimate the single point source performance in terms of sensitivity and position accuracy through the following procedures.

(1) Determine the flux threshold for point source detection.
   (a) Simulate a frame of observed data containing only background counts.
   (b) Run the denoising program on the simulated data to try to increase the SNR.
   (c) Demodulate the denoised data.
   (d) Run SExtractor, a source detection program by Bertin & Arnouts (1996), on the demodulated image to detect point sources and extract their intensities, coordinates and other parameters. At this point a catalog of point sources is compiled from the simulated data. Point sources detected here, i.e., from images demodulated from background data, are false detections.
   (e) Repeat the previous steps (from 1a to 1d) so that a series of catalogs are compiled. Draw a histogram of the flux of false detections that could possibly have been detected from background counts given a specific case of both observation and detection.
   (f) Choose a cut from the histogram as the flux threshold so that a certain percentage of the false detections are rejected and the rejection percentage is precise enough. The rejection percentage, e.g., 95% or 99.7% etc., should reflect the significance of detections above the corresponding threshold.

(2) Estimate detection efficiency and position accuracy of a point source that has a specific flux intensity.

(a) Simulate the observed data describing a single point source with a given flux intensity f_m located at (x_m, y_m) in the model image.
(b) Perform steps 1a to 1d. A catalog is compiled.
(c) Examine each detection in the catalog. Provided the $i-$th source in the catalog is detected at (x_i, y_i) in the demodulated image, the distance between the extracted source and the true point source

$$\delta_i = \sqrt{(x_m - x_i)^2 + (y_m - y_i)^2} \tag{7}$$

as well as the flux of the extracted source f_i are investigated to determine whether the $i-$th source is a true source or not. We define the score of the current catalog in detecting the single point source as

$$d_k = \begin{cases} 1 & \exists\, i : (\delta_i \leq \Delta) \wedge (f_i \geq F_{\rm thres}) \,, \\ 0 & \text{otherwise} \,, \end{cases} \tag{8}$$

where k is the index of the current catalog, and Δ and $F_{\rm thres}$ are position accuracy and flux threshold. Therefore the score d_k reveals whether the $k-$th catalog contains the true source or not, in other words, through the previous steps (simulated observation, denoising, demodulation, source extraction and thresholding), we can determine whether we have effectively detected the true source. If we have, the outcome of these steps is counted as an effective detection of the true source, otherwise it is ineffective.
(d) Repeat the previous steps (from 2a to 2c) N times and calculate the percentage of effective detections among all detections, namely,

$$\eta = \frac{1}{N} \sum_k^N d_k \,, \tag{9}$$

which is defined as the detection efficiency.
Let (x_k, y_k) be the position of the brightest source in the $k-$th catalog, then the position accuracy is calculated as

$$\rho = \frac{1}{\eta N} \sum_k^N d_k \sqrt{(x_k - x_m)^2 + (y_k - y_m)^2} \,. \tag{10}$$

(3) Find a flux intensity $F_{0.5}$ so that the corresponding detection efficiency $\eta = 50\%$. The intensity $F_{0.5}$ marks the point source sensitivity of the detecting system synthesized from both the telescope in specific status and the data analysis program.

2.2 Imaging and Mapping

2.2.1 Demodulation

The direct demodulation (DD) method (Li & Wu 1994) is used to estimate the true image from observed data. The residual map calculated with the CLEAN algorithm (Högbom 1974) is used as the lower-limit constraint in the DD method. The skewness of the residual map is calculated in each CLEAN iteration and its minimum absolute value serves as the main stopping criterion for iterations.

2.2.2 Cross-correlation

In addition to detecting and extracting point sources from demodulated images, it is also feasible to do so from cross-correlated maps as long as the point sources are isolated from each other. This can

be accomplished by comparing values of the full width at half maximum (FWHM) of the PSF, since the position of a peak of the expected value of such a map coincides with the position of a source regardless of the PSF. Cross-correlating the observed data and the PSF yields the correlated map

$$\boldsymbol{C} = \boldsymbol{D} \star \boldsymbol{H}, \tag{11}$$

where $\star$ denotes cross-correlation, and $\boldsymbol{D}$ and $\boldsymbol{H}$ denote the observed data and PSF respectively. According to Equation (6), the peak of $\boldsymbol{C}$ that coincides with a point source having flux intensity F is

$$C = \frac{\tau \cdot A \cdot F}{\max\limits_{i,j} H_{i,j}} \sum_{i,j} H_{i,j}^2 \,. \tag{12}$$

On the other hand, the background variance of the correlated map is

$$\sigma^2 \left(\boldsymbol{C}\right) = \sum_{i,j} \sigma^2 \left(\tau \cdot r_{\rm b} \cdot H_{i,j}\right) = \tau \cdot r_{\rm b} \cdot \sum_{i,j} H_{i,j}^2 \,, \tag{13}$$

since $\tau \cdot r_{\rm b}$ follows a Poisson distribution. Hence the significance of the peak in terms of numbers of σ is

$$\mathrm{SI} = \frac{F \cdot A \cdot \sqrt{\tau \cdot \sum_{i,j} H_{i,j}^2}}{\max\limits_{i,j} H_{i,j} \sqrt{r_{\rm b}}} = \frac{F \cdot A \cdot \sqrt{T}}{\sqrt{r_{\rm b}}} \sqrt{\langle P_{\rm tan}^2 \rangle} \,, \tag{14}$$

where T is total duration of the exposure on the 2-D pixel grid. $\sqrt{\langle P_{\rm tan}^2 \rangle}$ is the square root of the arithmetic mean of $P_{\rm tan}$ over the 2-D pixel grid, which is only determined by the PSF as well as the range of the pixel grid, provided that the pixel grid is fine enough (see Eq. (5)).

The cross-correlation significance of an isolated point source defined in Equation (14) can be evaluated directly, given only the flux intensity of the source, the background count rate, the duration of exposure, the detection area and the PSF. Hence it is determined by the object (i.e., the point source), the telescope and the status of observation; thus effects from data analysis programs are minimized.

We use the cross-correlation significance as a reference. For example, in our simulations an isolated point source with a $1\ \mathrm{mCrab}$ flux has a significance of 2.42σ.

2.3 Denoising

2.3.1 Linear methods

Gaussian smoothing is often used in digital image processing to suppress the noise at the cost of a reduction in resolution. The trade-off between noise suppression and maintaining a good resolution is adjusted through the standard deviation σ of the Gaussian distribution that acts as the smoothing kernel function. The best resolution of HXMT HE observed data is about 1.1°, which is limited by the FWHM of its narrow-field collimator. We set σ to $28'$ so that the FWHM of the Gaussian kernel is also 1.1°.

The $N-$fold cross-correlation ($N \geq 1$) can be used in the DD method to regularize the ill-posed problem; more specifically speaking, to ensure the convergence as well as stability of the solution (Li 2003). Here we put this technique in the denoising category. We have tested both $1-$fold and $2-$fold cross-correlated DD methods in this article.

2.3.2 Non-linear methods

Non-local means (NLMeans) denoising (Buades et al. 2005) is an edge-preserving non-linear denoising method. To increase its performance we have implemented this method with fast Fourier transforms (FFTs). The pixel-wise evaluation of the general Euclidean distance between the $i-$th pixel and other pixels in an image is replaced by

$$\boldsymbol{D}_i = \left\{ \sum_k N_{i,k} \cdot W_k + \left(I^2 * W\right) - 2\left[I * (N_i \cdot W)\right] \right\}^{\frac{1}{2}}, \tag{15}$$

where N_i is a neighborhood associated with the i-th pixel, $N_{i,k}$ is the k-th pixel in the neighborhood, I is the image, and W is the weight coefficient of the distance function. We use a 7×7 pixel Gaussian kernel with standard deviation $\sigma = 2$ (in pixels) as the weight coefficient W in our simulations. We reduce the complexity of the NLMeans method by computing convolutions in Equation (15) with FFTs instead of using searching windows (Buades et al. 2008).

A median filter is another non-linear edge-preserving denoising method. This method is effective in removing salt-and-pepper noise in digital images. In data observed by HXMT, such noise is typically incurred by missing data or detections of cosmic rays. We fixed the size of the filter at $2^\circ \times 2^\circ$ (about 50×50 pixels) in the denoising process for HXMT HE data.

The last non-linear denoising method included in this article is adaptive wavelet thresholding with multiresolution support (Starck & Murtagh 2006). The multiresolution support of a noisy image is a subset that only contains significant coefficients. So, wavelet coefficients that are dominated by noise are discarded. In this article we implemented the algorithm in a non-iterative was. The 5×5 B_3 spline wavelet is used for multiresolution decomposition.

3 SIMULATION AND RESULTS

3.1 In-orbit Background Simulation

The HXMT HE in-orbit background count rate $r_{\rm b}$ ranges from $147.6\,{\rm counts\,s^{-1}}$ to $210.7\,{\rm counts\,s^{-1}}$ (Li et al. 2009). We use a constant count rate of $180\,{\rm counts\,s^{-1}}$ to simulate the average in-orbit background of HXMT HE in this article.

3.2 Source Energy Spectrum and Telescope Detection Efficiency

We use the formula proposed by Massaro et al. (2000) together with parameters fitted by Jourdain & Roques (2009)

$$F(E) = 3.87 \times E^{-1.79-0.134\log_{10}(E/20)} \tag{16}$$

to model energy spectra of Crab-like sources from 20 keV to 250 keV, where E is in keV and the flux $F(E)$ is in ${\rm photons\,s^{-1}\,cm^{-2}\,keV^{-1}}$.

The detector efficiency of HXMT HE is derived from its simulated energy response, as shown in Figure 1.

Detection efficiency of HXMT HE to a Crab-like source is 67%. Given the detection area of HXMT HE is about $5100\,{\rm cm^2}$, the count rate of HXMT HE corresponding to the intensity of $1\,{\rm Crab}$ is $1112\,{\rm counts\,s^{-1}}$.

3.3 PSF and Modulation

We use the diagram shown in Figure 2 to simulate the PSF $P_{\tan}(u,v)$ on the tangent plane.

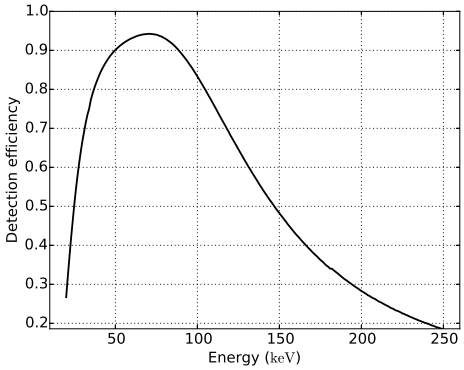

Fig. 1 HXMT HE detection efficiency.

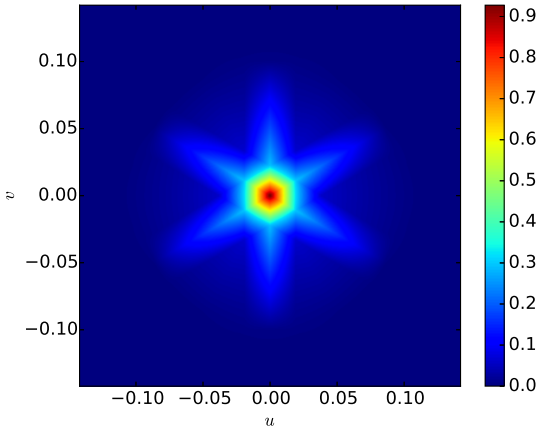

Fig. 2 Simulated HXMT HE PSF.

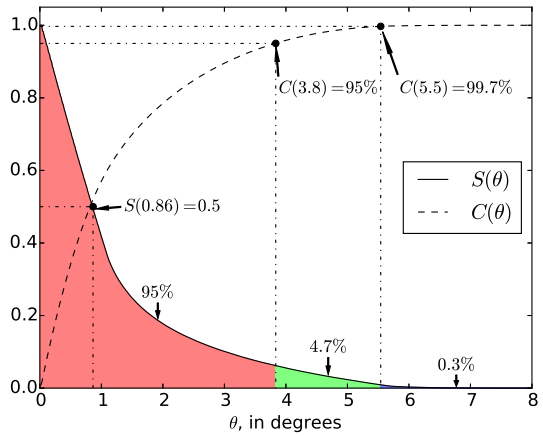

Fig. 3 Radial distribution of the simulated HXMT HE PSF.

Table 1 2σ and 3σ Thresholds of Point Source Detection

Denoising	2σ thres. (mCrab)	3σ thres. (mCrab)
w/o denoise	0.520 ± 0.001	0.963 ± 0.003
1-fold CCT	0.667 ± 0.003	1.192 ± 0.010
2-fold CCT	0.919 ± 0.014	1.656 ± 0.058
Gaussian, $\sigma = 28'$	0.669 ± 0.003	1.133 ± 0.008
NLMeans	0.845 ± 0.004	1.340 ± 0.011
Median filter, 2°	0.709 ± 0.004	1.185 ± 0.015
Median filter, 4°	0.665 ± 0.005	1.114 ± 0.012
Wavelet thres.	0.0518 ± 0.0002	0.216 ± 0.002

We use the concentric average of $P(\phi, \theta)$, namely,

$$S(\theta) = \frac{\int_{-\pi}^{\pi} P(\phi, \theta) \mathrm{d}\phi}{2\pi}, \tag{17}$$

and the cumulative sum of $S(\theta)$,

$$C(\theta) = \int_0^\theta S\left(\theta'\right) \mathrm{d}\theta' \tag{18}$$

to characterize the radial fade-out of the PSF and the concentration of the PSF respectively, as plotted in Figure 3.

From Figure 3 we see that the FWHM of the simulated PSF is about 1.7° while 99.7% of responses occur in a diameter of 11°.

Despite the fact that the directly observed data are scientific events instead of 2-dimensional images, we start our simulation from *simulated* data in the form of images defined on a 2-dimensional Cartesian pixel grid. We use a $22^\circ \times 22^\circ$ model image for simulations. Given the diameter of the PSF, the central $11^\circ \times 11^\circ$ region is fully modulated, that is, all contributions to observed data in this region are only from the model image. The surrounding $33^\circ \times 33^\circ$ region is partially modulated, i.e., part of the contributions to observed data in this region are from the model image.

The average exposure per unit solid angle is 382 s deg^{-2} in the HXMT half-year all-sky survey. The partially modulated region is discretized by an $N \times N$ pixel grid, so $\tau \approx 382 \times 33^2/N^2$. The detection area of each HXMT HE detector is approximately $300\ \mathrm{cm}^2$ so the total area of all the 17 HXMT HE detectors is $5100\ \mathrm{cm}^2$.

3.4 Results

We have implemented several denoising methods (see Sect. 2.3). Figure 4 shows denoising results by these methods.

We have simulated 5000 frames of observed data that only contain the in-orbit background counts for each method to estimate the corresponding flux thresholds by the method specified in Procedure 2a of Section 2.1. From false detections, we have obtained 2σ and 3σ flux thresholds, see Table 1 for results.

We have simulated 1000 frames of observed data that contain a Crab-like point source with intensity 1, 1.25, 1.5, 1.75, 2, 2.5, 3, 4, 5 and 10 mCrab, i.e., there are $10\,000$ frames of observed data in total.

With these simulated data we have estimated the location accuracies as well as detection efficiencies by applying Procedure 2a with the following methods:

– DD without denoising,
– DD with 1-fold cross-correlation,

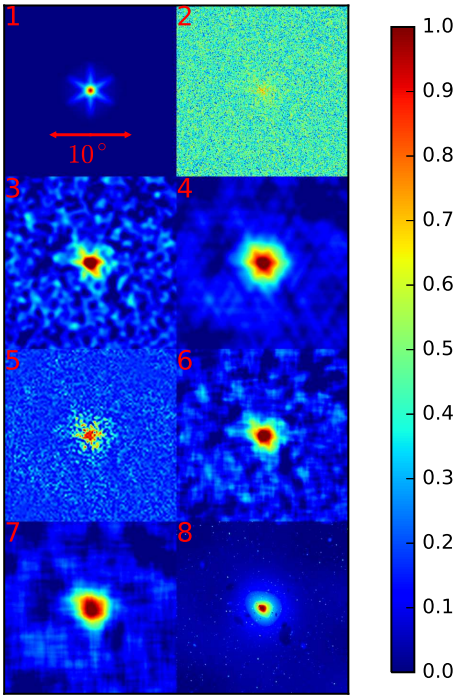

Fig. 4 Denoising methods. From top to bottom and left to right: 1. Model image; 2. Observed data of a $10\ \mathrm{mCrab}$ point source. 3. Gaussian smoothed data, $\sigma = 28'$. 4. 1-fold cross correlated data. 5. NLMeans filter denoised data. 6. $2^\circ \times 2^\circ$ median filter denoised data. 7. $4^\circ \times 4^\circ$ median filter denoised data. 8. 3σ wavelet thresholding denoised data, with B_3 spline wavelet transform.

- DD with 2-fold cross-correlation,
- DD with Gaussian smoothing, where $\sigma = 28'$,
- DD with NLMeans filtering, the size of the filter is 7×7 and $\sigma = 2$ (both parameters are in pixels),
- DD with $2^\circ \times 2^\circ$ median filter,
- DD with $4^\circ \times 4^\circ$ median filter, and
- DD with adaptive wavelet thresholding.

Details describing the implementation of the above methods are in Section 2.3.

Table 2 shows the location accuracies on simulated data of 1, 2, 5 and 10 mCrab point sources.

Table 3 shows the detection efficiencies on simulated data of 1, 1.5, 2, 2.5 and 3 mCrab point sources.

Although the RL iteration itself we employed in the DD method conserves the total counts, i.e., the sum of counts of each pixel is conserved after the iteration (Richardson 1972), the regularizations including the background constraints as well as various denoising techniques are not necessarily count-conservative. As a result, the absolute flux threshold (Table 1) for rejecting false detections does not directly reflect the sensitivity but the detection efficiency (Table 3) does.

Errors in flux thresholds, location accuracies and detection efficiencies in Table 1, Table 2 and Table 3 are calculated by bootstrapping. For example, following Procedure 2a a set of 5000 frames of demodulated images is obtained, from which false detections are calculated and a histogram is

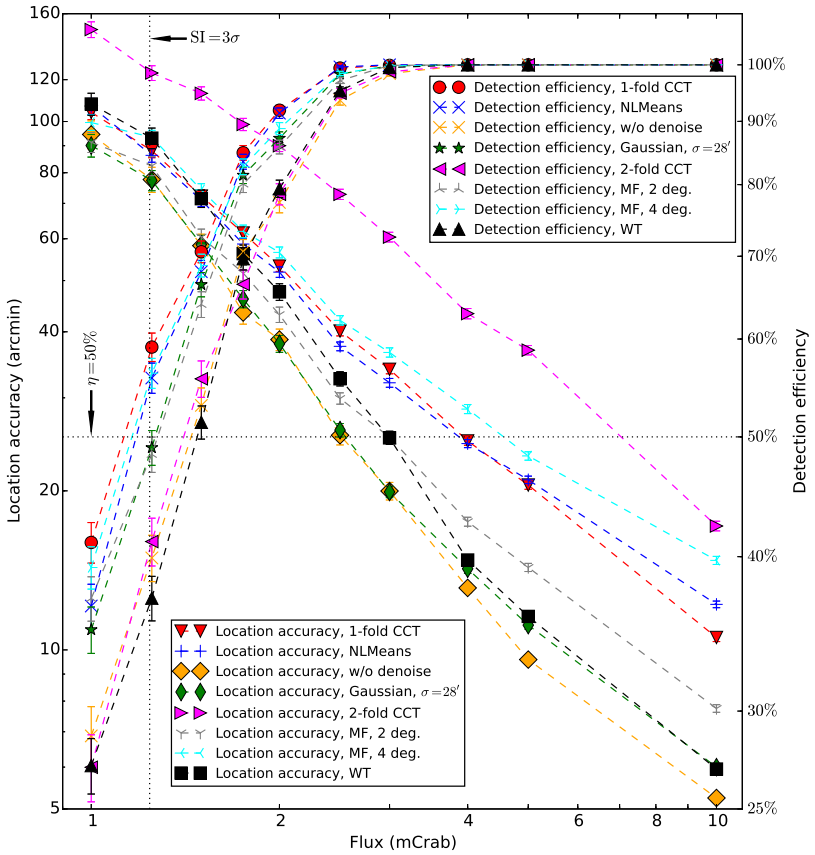

Fig. 5 Single source location accuracy and detection efficiency. MF stands for the median filter while WT for wavelet thresholding.

Table 2 Location Accuracies (in arcmin)

	1 mCrab	2 mCrab	5 mCrab	10 mCrab
w/o denoise	95 ± 6	39 ± 2	9.6 ± 0.2	5.2 ± 0.1
1-fold CCT	104 ± 3	53 ± 1	20.5 ± 0.4	10.6 ± 0.2
2-fold CCT	149 ± 5	90 ± 2	36.9 ± 0.8	17.2 ± 0.4
Gaussian, $\sigma = 28'$	90 ± 4	38 ± 1	11.1 ± 0.2	6.0 ± 0.1
NLMeans	107 ± 4	52 ± 1	21.0 ± 0.3	12.2 ± 0.2
Median filter, 2°	91 ± 4	43 ± 1	14.3 ± 0.3	7.7 ± 0.1
Median filter, 4°	100 ± 3	57 ± 1	23.3 ± 0.4	14.8 ± 0.3
Wavelet thres.	108 ± 5	48 ± 2	11.6 ± 0.2	5.9 ± 0.1

plotted, where both the 2σ and 3σ thresholds are determined. Now let us generate a new set with the same volume by resampling from the original set with replacement in order to calculate both thresholds again. We repeat this resampling process until we get enough calculated thresholds to estimate their standard deviations. In Table 1, Table 2 and Table 3, each of the errors is expressed as a standard deviation that is calculated from 1000 resampled sets.

Table 3 Detection Efficiencies (in percentage)

	1 mCrab	1.5 mCrab	2 mCrab	2.5 mCrab	3 mCrab
w/o denoise	29 ± 2	53 ± 2	77 ± 1	94 ± 1	98 ± 0
1-fold CCT	41 ± 2	71 ± 1	92 ± 1	99 ± 0	100 ± 0
2-fold CCT	27 ± 2	56 ± 2	79 ± 2	95 ± 1	99 ± 0
Gaussian, $\sigma = 28'$	35 ± 2	66 ± 2	87 ± 1	98 ± 0	100 ± 0
NLMeans	36 ± 2	68 ± 1	91 ± 1	100 ± 0	100 ± 0
Median filter, 2°	37 ± 2	64 ± 2	86 ± 1	97 ± 1	100 ± 0
Median filter, 4°	39 ± 2	69 ± 1	89 ± 1	98 ± 0	100 ± 0
Wavelet thres.	27 ± 1	51 ± 2	79 ± 1	95 ± 1	100 ± 0

A comprehensive summary of all the tested methods on all simulated data is shown in Figure 5.

4 CONCLUSIONS

According to the results from our tests, no denoising method shows a significant advantage over the 1-fold cross-correlated DD method in single point source detection efficiency. Therefore it is suggested that 1-fold cross-correlation should be the default regularization method for single point source detection in HXMT imaging data analysis.

On the other hand, the location accuracy can be improved with alternative denoising methods, such as a median filter, wavelet thresholding, Gaussian smoothing with a smaller kernel, or without denoising, according to the results in this work.

This article is focused on the single point source detection that is part of HXMT imaging data analysis, so other interesting topics related to this study cannot all be covered. Although alternative denoising methods have been out-performed more or less by the default 1-fold cross-correlation in terms of their contributions to the detection efficiency, they have shown certain advantages in location accuracy. These features are promising for locating bright transients, resolving multiple sources, and so on.

Acknowledgements In this work we made use of SciPy (Jones et al. 2001–), PyFITS and AIRE. PyFITS is a product of the Space Telescope Science Institute, which is operated by AURA for NASA. AIRE is a set of computing facilities administered by the Tsinghua Centre for Astrophysics. This work was supported by the National Natural Science Foundation of China (NSFC, Grant Nos. 11373025, 11173038 and 11403014) as well as the Tsinghua University Initiative Scientific Research Program (Grant No. 20111081102). This work was also supported by the Young Scientist Project of the National Natural Science Foundation of China (Grant No. 11303059) and the Chinese Academy of Sciences Youth Innovation Promotion Association.

References

Bertin, E., & Arnouts, S. 1996, A&AS, 117, 393

Buades, A., Coll, B., & Morel, J.-M. 2005, in Computer Vision and Pattern Recognition, 2005. CVPR 2005. IEEE Computer Society Conference on, 2, IEEE, 60

Buades, A., Coll, B., & Morel, J.-M. 2008, International Journal of Computer Vision, 76, 123

Högbom, J. A. 1974, A&AS, 15, 417

Huo, Z.-X., & Zhou, J.-F. 2013, RAA (Research in Astronomy and Astrophysics), 13, 991

Jin, J., Chen, Y., Zhang, S.-N., et al. 2010, Chinese Physics C, 34, 66

Jones, E., Oliphant, T., Peterson, P., et al. 2001–, SciPy: Open Source Scientific Tools for Python, *http://www.scipy.org/*

Jourdain, E., & Roques, J. P. 2009, ApJ, 704, 17

Li, G., Wu, M., Zhang, S., & Jin, Y.-K. 2009, Chinese Astronomy and Astrophysics, 33, 333
Li, T. P. 2003, in IAU Symposium, Vol. 214, High Energy Processes and Phenomena in Astrophysics, eds. X. D. Li, V. Trimble, & Z. R. Wang, 70
Li, T.-P. 2007, Nuclear Physics B Proceedings Supplements, 166, 131
Li, T.-P., & Wu, M. 1994, Ap&SS, 215, 213
Lu, F. 2012, in Society of Photo-Optical Instrumentation Engineers (SPIE) Conference Series, 8443, Society of Photo-Optical Instrumentation Engineers (SPIE) Conference Series, 1
Massaro, E., Cusumano, G., Litterio, M., & Mineo, T. 2000, A&A, 361, 695
Richardson, W. H. 1972, Journal of the Optical Society of America (1917–1983), 62, 55
Starck, J.-L., & Murtagh, F. 2006, Astronomical Image and Data Analysis (Berlin: Springer-Verlag)